

Effects of the Centrifugal Pump Outlet Blade Angle on Its Internal Flow Field Characteristics under Cavitation Condition

Y. Y. Wang¹, W. G. Zhao^{1†}, X. D. Han², P. J. Fan³, Z. L. Liu¹ and J. Q. Hu³

¹ College of Energy and Power Engineering, Lanzhou University of Technology, Lanzhou, 730050, China

² School of Civil Engineering, Nanchang Institute of Technology, Nanchang, 330044, China

³ Machine Industry Lanzhou Petrochemical Equipment Inspection Institute Co., LTD, Lanzhou, 730070, China

†Corresponding Author Email: zhaowg@zju.edu.cn

(Received April 21, 2022; accepted September 29, 2022)

ABSTRACT

The outlet blade angle is a key geometrical parameter that governs how the impeller directly influences centrifugal pump performance. Therefore, a reasonable angle selection is crucial. To investigate the effects of the outlet blade angle on centrifugal pump internal flow field characteristics under cavitation conditions, this study employs a combination of a modified SST $k-\omega$ turbulent model with a Zwart-Gerber-Belamri cavitation model to perform transient flow simulations. Outlet blade angles of 15°, 20°, 25°, 30°, and 35° were tested. The results indicated that as the outlet blade angle increased, the relative liquid flow angle, vapor volume, and corresponding fraction first increased, then decreased, and finally increased again. Meanwhile, the distribution scope of each stall vortex on the suction surface became smaller, then larger, and smaller again, whereas the scopes of the pressure surfaces grew constantly as the outlet blade angle increased. Pressure fluctuations at all monitored points in the volute became weaker over time, and variations in the pressure fluctuations alternated with the outlet blade angle. The main frequency amplitude increased and the frequency doubling decreased as the outlet blade angle increased. Although the energy corresponding to the main frequency was unstable, it consistently held the dominant position. The duration that cavitation compliance was less than 0 first decreased and then increased as the outlet blade angle increased. For the impeller with an outlet blade angle of 25°, stall vortices accounted for the smallest regions, and the duration of negative cavitation compliance was minimized. In this case, the overall performance of the centrifugal pump was optimal.

Keywords: Centrifugal pump; Outlet blade angle; Cavitation; Net positive suction head available; Net positive suction head required; Computational fluid dynamics.

NOMENCLATURE

| | | | |
|-------|--------------------------|-----------|-------------------------------------|
| b_2 | impeller outlet width | n_s | specific speed |
| b_3 | volute inlet width | $NPSH_a$ | net positive suction head available |
| C_p | pressure coefficient | Q | flow rate |
| D_s | pump inlet diameter | Q_d | design flow rate |
| D_d | pump outlet diameter | Q/Q_d | relative flow rate |
| D_j | impeller inlet diameter | t | time |
| D_2 | impeller outlet diameter | Z | blade number |
| D_3 | base circle diameter | β_1 | inlet blade angle |
| D_4 | volute outlet diameter | β_2 | outlet blade angle |
| H | head | φ | blade wrap angle |
| K | cavitation compliance | η | efficiency |

1. INTRODUCTION

Centrifugal pumps are important components of hydraulic machinery (Su *et al.* 2021), and they are

widely employed in various engineering fields. When the local pressure is less than the saturated vapor pressure, cavitation (a type of complex multiphase flow) may occur in the centrifugal pump (Ennouri *et al.* 2019). Under most operating

conditions, cavitation induces harmful effects and can have detrimental consequences. Cavitation causes intense variations in dynamic performance, thereby destabilizing the internal flow. Meanwhile, the operation efficiency of the centrifugal pump decreases significantly (Grist 1998). Additionally, cavitation erosion can trigger destruction of the blade surfaces, leading to long-term damage (Biryukov *et al.* 2022).

The geometrical parameters of an impeller have a significant effect on the centrifugal pump's internal flow field characteristics and variations. Numerous investigations have focused on these relationships. For example, Elyamin *et al.* (2019) discussed the effects of different numbers of blades on one centrifugal pump's performance. They found that the head and efficiency were higher with seven blades relative to five or nine blades. Matlakala *et al.* (2019) performed numerical simulations to study the effects of various blade diameters (2000, 2200, and 2400 mm) on centrifugal pump hydraulic performance. As the blade diameter increased, the head and flow rate also increased gradually. Donmez *et al.* (2019) presented parametric discussions regarding the role of the inlet blade angle on the centrifugal pump cavitation performance. They observed that upon increasing the shroud blade angle from 20° to 30°, the performance improved significantly. However, further increasing the angle from 30° to 50° led to an opposite variation. Moreover, increasing the hub blade angle had a negative effect on the performance. Shi *et al.* (2013) examined the effects of different impeller outlet widths (9, 10, 11, and 12 mm) on deep-well centrifugal pump performance. As the outlet width increased, the head and power of single stage also increased gradually. Moreover, optimal efficiency was observed under high flow rate conditions, and the efficiency value decreased. Wang *et al.* (2016) analyzed the impact of various turbine blade inlet widths (13, 16, and 19 mm) on centrifugal pump performance. As the width increased, the flow rate, efficiency, shaft power, and pressure head all increased. Bozorgasareh *et al.* (2021) investigated how impellers with different bladelets affected the centrifugal pump hydraulic performances. Their results indicated that an impeller with a 90° bladelet angle exhibited significantly enhanced performance.

The outlet blade angle is another critical parameter that can influence centrifugal pump internal flow field characteristics. Bacharoudis *et al.* (2008) evaluated centrifugal pump hydraulic performances with various outlet blade angles. They observed that the performance curves became smoother and flatter as the outlet blade angle increased. Mohammadi and Fakharzadeh (2017) studied the effects of various outlet blade angles on the hydraulic performance of a multi-pressure pump. Numerical and experimental results revealed that maximal head and efficiency were obtained with an outlet blade angle of 30°. Shigemitsu *et al.* (2011) discussed the effects of the outlet blade angle on a mini centrifugal pump's internal flow fields and hydraulic performance; they found that head

increased gradually as the outlet blade angle increased and the blade thickness decreased. Shojaeefard *et al.* (2012) evaluated the role of the outlet blade angle in governing the variations in the centrifugal pump head and efficiency; both of these parameters improved at an outlet blade angle of 30° compared with 32.5° of angles <27.5°. Zhang *et al.* (2020) analyzed the radial force variations of impellers with different outlet blade angles. The force increased as the outlet blade angle increased under constant flow rate conditions. Peng *et al.* (2020) discussed the influence of the outlet blade angle in preventing overload in a centrifugal pump. Their results indicated that the power curve could be controlled to restrain the overload by appropriately reducing the outlet blade angle.

However, under cavitation conditions, the effects of different outlet blade angles on the centrifugal pump internal flow field characteristics require further investigations. This report describes numerical simulations of cavitation flow in a low (specific) speed centrifugal pump with various outlet blade angles. We evaluated variations in hydraulic and cavitation performances, distributions of stall vortices, pressure fluctuation, and centrifugal pump stability to determine the degree to which the outlet blade angle affects centrifugal pump internal flow field characteristics under cavitation conditions.

2. THEORETICAL BACKGROUND

2.1 Fundamental Equations

In the numerical simulations, water is the primary phase and vapor is the secondary phase, together comprising a homogeneous fluid. Phase change occurred between water and vapor. The continuity, momentum, and transportation equations used in this work (Ferziger *et al.* 2019) are expressed in Eqs. 1-3, respectively,

$$\frac{\partial \rho_m}{\partial t} + \frac{\partial (\rho_m u_j)}{\partial x_j} = 0 \quad (1)$$

$$\frac{\partial (\rho_m u_i)}{\partial t} + \frac{\partial (\rho_m u_i u_j)}{\partial x_j} = -\frac{\partial p}{\partial x_i} + \frac{\partial}{\partial x_j} \left(\mu_m \frac{\partial u_i}{\partial x_j} \right) \quad (2)$$

$$\frac{\partial (\rho_m \alpha_v \alpha_i)}{\partial t} + \frac{\partial (\rho_m \alpha_v u_j)}{\partial x_j} = m^+ - m^- \quad (3)$$

where ρ_m is the mixture density, kg/m³; u is the mixture velocity, m/s; x is the coordinate; subscripts i and j are between 1-3; t is time, s; p is pressure, Pa; μ_m is the mixture dynamic viscosity, N·s/m²; α_v is the vapor volume fraction; m^+ is the evaporation source term; and m^- is the condensation source term.

2.2 Turbulence Model

An SST $k-\omega$ turbulence model is employed to determine the turbulent flow in the low (specific) speed centrifugal pump. This model combines the advantages of near-wall treatments of a $k-\omega$ model and the ability to solve the outer region of a $k-\varepsilon$ model. Moreover, this model accounts for turbulent

shear stress transportation and can therefore provide a detailed prediction of flow separation under various pressure gradient conditions. Therefore, the SST $k-\omega$ model is suitable for predicting high rotational speeds and strong separate flows (Wilcox 1994, Wilcox 2008). Overall, the precision and credibility of this approach are high.

However, the density gradient is particularly sharp in the cavitation region, which means that there is compressible two-phase flow. Therefore, a general SST $k-\omega$ turbulence model for fully incompressible flow cannot accurately predict cavitation evolution. Thus, the model was modified according to the density function $f(\rho)$ defined in Eq. 4,

$$f(\rho) = \rho_v + \frac{(\rho_m - \rho_v)^n}{(\rho_1 - \rho_v)^{n-1}} \quad n \geq 1 \quad (4)$$

And the turbulence viscosity μ_t defined in Eq. 5,

$$\mu_t = f(\rho) \frac{k}{\omega} \quad (5)$$

where ρ_v is the vapor density; k is the turbulent kinetic energy; ω is the dissipation frequency; and n is a constant (herein taken as 10) (Coutier-Delgosh *et al.* 2003). This modified method has been verified and validated using diverse cases, e.g., cavitating flow in a Venturi tube (Decaix and Goncalves 2013) and around the hydrofoil (Dular *et al.* 2007).

As shown in Table 1, user-defined formulas are input to the equation editor built into the CFX system. Specifically, the formula *mut* is loaded via the pathway, “Flow Analysis1→Fluid Models→Advanced Turbulence Control→Eddy Viscosity”, to appropriately modulate the viscosity coefficient in the SST $k-\omega$ turbulence model.

Table 1. User-defined formulas

| Name | Formula |
|------------|---|
| ρ_v | 0.02308 kg·m ⁻³ |
| ρ_1 | 997 kg·m ⁻³ |
| α_v | Vapor volume fraction |
| k | Turbulence kinetic energy |
| ω | Specific dissipation rate |
| <i>mut</i> | $(\rho_v + (\rho_1 - \rho_v) * (1 - \alpha_v)^{10}) * (k/\omega)$ |

2.3 Cavitation Model

The Zwart-Gerber-Belamri (Z-G-B) cavitation model (Zwart *et al.* 2004) is employed to simulate phase changes. This model assumes that the density of cavitation nuclei remains constant. The flow parameters are the weighted averages of two-phase (i.e., water-vapor) flow parameters. The source terms are defined as shown in Eqs. 6 and 7,

$$m^+ = C_c \frac{3\alpha_{nuc}(1-\alpha_v)\rho_v}{R_b} \sqrt{\frac{2}{3} \frac{p_v - p}{\rho_1}} \quad p < p_v \quad (6)$$

$$m^- = C_c \frac{3\alpha_v\rho_v}{R_b} \sqrt{\frac{2}{3} \frac{p - p_v}{\rho_1}} \quad p > p_v \quad (7)$$

where R_b is the cavitation bubble radius (1×10^{-6} m); p_v is the saturated vapor pressure; α_{nuc} is the cavitation nucleus density (herein taken as 5×10^{-4}); and C_e and C_c are empirical coefficients, which are equal to 50 and 0.02, respectively.

3. NUMERICAL SIMULATION SETUP

3.1 Physical Model

A low (specific) speed centrifugal pump refers to a centrifugal pump with a specific speed of $n_s = 30-80$ (Chen *et al.* 2022). The performance parameters of the centrifugal pump used in this work include the flow rate $Q = 8.6$ m³/h, head $H = 4.0$ m, efficiency $\eta = 42\%$, and specific speed $n_s = 32$. The main geometrical parameters are presented in Table 2.

To investigate the effects of different outlet blade angles on the centrifugal pump’s internal flow field characteristics under cavitation conditions, we evaluate various angles: 15°, 20°, 25°, 30°, and 35°. In the numerical simulations, the corresponding centrifugal pump models are labeled as M₁, M₂, M₃, and M₄, respectively, and the original pump model is denoted as M₀.

Table 2. Main geometrical parameters of the original low-speed centrifugal pump (M₀)

| Parameter | Value | Parameter | Value |
|-----------|-------|-----------|-------|
| D_s | 90 | β_2 | 25 |
| D_d | 65 | φ | 175 |
| D_j | 85 | Z | 6 |
| D_2 | 310 | D_3 | 320 |
| b_2 | 12 | b_3 | 22 |
| β_1 | 37 | D_4 | 350 |

3.2 Mesh Generation

Hexahedral structured meshes are generated using ANSYS-ICEM to enable the discretization of the centrifugal pump computational domain. The benefit of this approach is its high solution efficiency, which shortens the computation time. To ensure accuracy, y^+ is introduced to capture boundary layer flow details (Tu *et al.* 2007). For the SST $k-\omega$ turbulence model, the value of y^+ should be less than 1; in the present study, the maximum value is 0.5. The physical models of various components and the corresponding meshes are depicted in Figs. 1 and 2, respectively.

Model M₀ is used as an example to perform a mesh independence check and sensitivity analysis. As shown in Table 3, the head gradually increases at first and then decreases as the total number of elements increases. Variations in efficiency followed an identical trend. The maximum relative errors for head and efficiency are <0.97% and <1.7%, respectively. These findings indicate that the total number of elements has a negligible effect on the numerical simulation results. To optimize

the computing resources, Scheme C (number of elements = 2365846) is selected for subsequent numerical simulations.

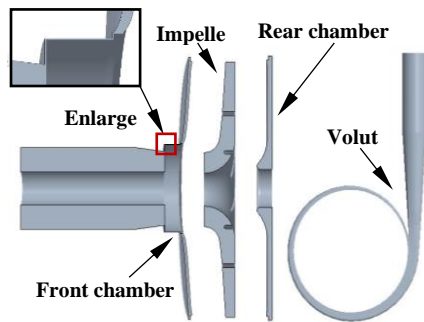


Fig. 1. Physical model of the low (specific) speed centrifugal pump components.

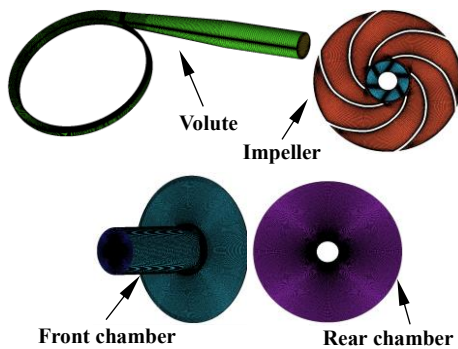


Fig. 2. Generated meshes of key components.

Table 3. Mesh independence check and sensitivity analysis.

| Scheme | Total number of elements | H | η |
|--------|--------------------------|------|--------|
| A | 2070238 | 4.12 | 55 |
| B | 2161665 | 4.13 | 56 |
| C | 2365846 | 4.17 | 57 |
| D | 2481249 | 4.15 | 59 |
| E | 2601985 | 4.13 | 57 |

3.3 Boundary Conditions and Numerical Simulation Methods

Numerical simulations of the transient cavitation flow inside the centrifugal pump are performed using the commercial software, CFX. The static pressure and the mass flow rate are set as inlet and outlet boundary conditions, respectively. The inlet pressure is modulated to simulate various degrees of cavitation development. The saturated vapor pressure is set as 3540 Pa, and the vapor volume fraction is assumed to be 0 at the centrifugal pump inlet. All wall surfaces are non-slip. For the steady simulation, the interface between the rotating and stationary domains is set as a frozen rotor.

A finite volume method is applied to discretize the governing equations, and the advection term is solved via high-resolution discretization. The

turbulence numeric is solved using a second-order model. Steady results are taken as the initial conditions for transient simulations. The transient is then solved using a second-order backward Euler function. The time required for a 3° rotation of the impeller is set as the time step (here, 0.001 s). When the monitored parameters exhibited periodic changes, the results could be used for transient investigations.

4. ALGORITHM VERIFICATION AND VALIDATION

Cavitation performance experiments for the original centrifugal pump are conducted, and the experimental results are compared with the analogous numerical simulations to verify and validate the reasonableness and robustness of the constructed algorithm.

The experimental rig (Fig. 3) comprised a motor, torque meter, visualized centrifugal pump, vacuum pump, inlet/outlet pressure gauges, electromagnetic flow meter, valve, water ring vacuum pump, water tank, and vacuum meter.

Figure 4a shows the model centrifugal pump and Fig. 4b depicts the impeller. High-precision sensors are employed to ensure credible experimental results. The key parameters related to these devices are presented in Table 4.

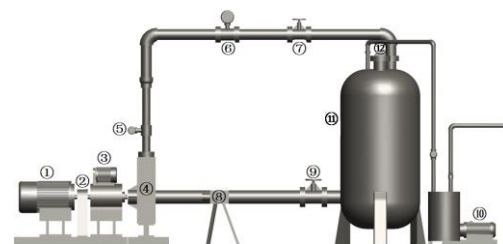


Fig. 3. Schematic picture of the experimental rig.

These experiments reveal the head and efficiency under designed operating conditions and the head under cavitation conditions for the model centrifugal pump, as shown in Figs. 5 and 6, respectively. Meanwhile, corresponding numerical simulations are carried out to enable quantitative and qualitative comparisons. Under designed operating conditions, the maximum relative error for head is < 2% and that for efficiency is 2.3%. Notably, these errors are only 0.6% and 1.2%, respectively, under the designed operating conditions. Under cavitation conditions the error for head is 3.2%. They agree well. Moreover, the simulated distributions of cavitation bubbles under different net positive suction head available ($NPSH_a$) conditions are consistent with the corresponding experimental outcomes, as shown in Fig. 7. The developed numerical algorithm therefore exhibited high reasonableness.



Fig. 4. Physical models of the experimental centrifugal pump: (a) original centrifugal pump; (b) impeller.

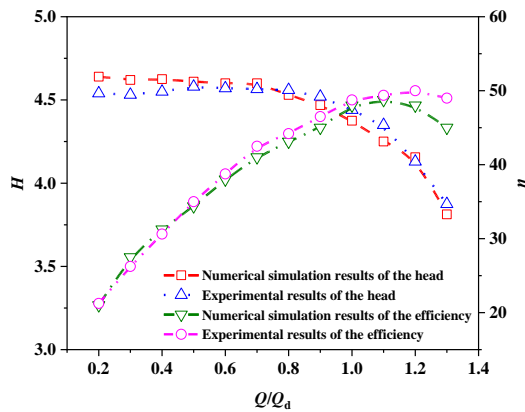


Fig. 5. Hydraulic performance curves under designed operating conditions.

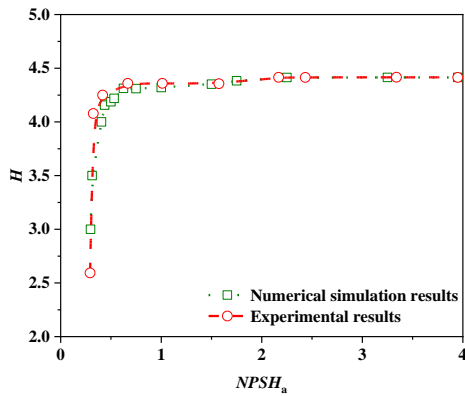


Fig. 6. Cavitation performance curves.

5. RESULTS AND DISCUSSION

5.1 Variations of Hydraulic and Cavitation Performances

Figure 8 shows the variations in the head and efficiency of the centrifugal pump with five outlet blade angles under diverse flow rates and designed operating conditions. The outlet blade angle has a significant effect on the centrifugal pump's hydraulic performance relative to the original configuration. The head varies between -7.1% and $+5.36\%$. Under identical flow rates, the head increases as the outlet blade angle increases. The main reason for this phenomenon is that the

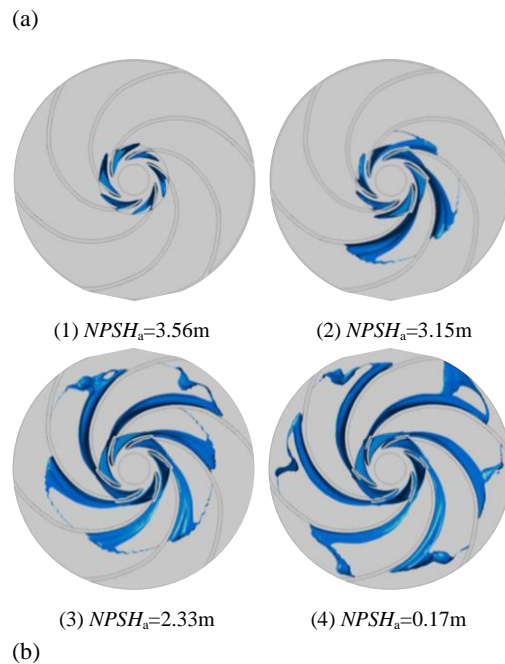
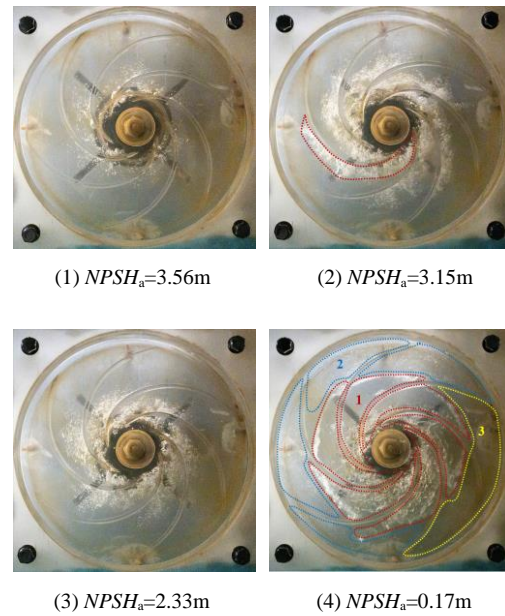


Fig. 7. Distribution of cavitation bubbles in the impeller: (a) experimental results; (b) numerical simulation results.

Table. 4 Parameters for devices

| Device | Position | Type | Accuracy (%) | Range |
|-----------------|-------------|-----------|--------------|--------------------------|
| Pressure gauge | Inlet | Pressure | ± 0.25 | 0.1-0.1 MPa |
| | Outlet | Pressure | ± 0.25 | 0-1.6 MPa |
| Flow gauge | Outlet | Flow rate | ± 0.5 | 3.5-50 m ³ /h |
| Torque detector | Motor shaft | Speed | ± 0.2 | 0-800 r/min |
| | Motor shaft | Torque | ± 0.2 | 0-50 N·m |

dynamic head and absolute velocity circumferential component at the impeller outlet increases with increasing outlet blade angle. The efficiency varies between -4.1% and $+4.16\%$ and generally decreases as the outlet blade angle increases under all flow rate conditions. The primary reason for this is that the flow channels between different blades become shorter and more curved as the angle increases, thereby increasing the diffusion angles between adjacent blades. These relationships result in significant hydraulic losses.

Similar variations in terms of head and efficiency are observed as a function of $NPSH_a$ under cavitation conditions, as shown in Fig. 9. For identical $NPSH_a$, the head increases and efficiency decreases as the outlet blade angle increases. Compared with the original centrifugal pump, the head varies between -4.24% and 4.15% and efficiency varies between -6.79% and 7.81% . As the outlet blade angle increases, the $NPSH_a$ remains under 3% when the head drop conditions are 0.048, 0.047, 0.039, 0.042, and 0.05 m, respectively. The impeller with an outlet blade angle of 25° exhibits the best cavitation performance.

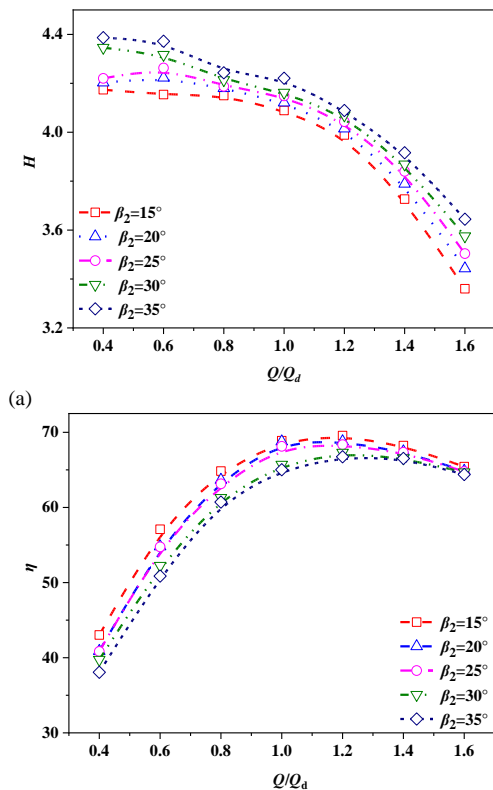


Fig. 8. Variations in (a) head and (b) efficiency under designed operating conditions.

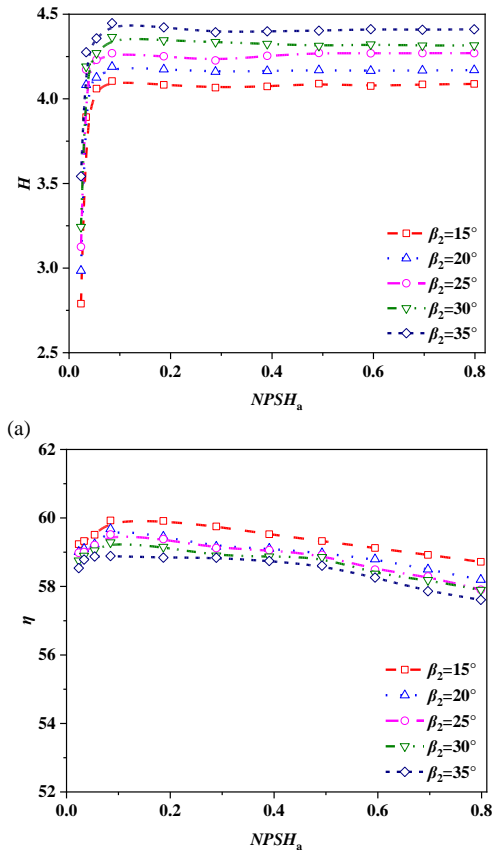


Fig. 9. Variations in (a) head and (b) efficiency under cavitation conditions.

Owing to the limited control of the blades, liquid movement trajectories have certain deviations. Nevertheless, the relative liquid flow angle has less of an impact than outlet blade angle on cavitation performance. Five schemes are analyzed to evaluate the effects of relative liquid flow angles on cavitation performance in the presence of various outlet blade angles. As shown in Fig. 10, when outlet blade angle increases from 15° to 35° , the relative liquid flow angle increases, then decreases, and increases again. The vapor volume and vapor volume fraction exhibit analogous trends.

5.2 Variations in the Distributions of Stall Vortices

Figure 11 shows the distribution of stall vortices in the impeller middle span with $NPSH_a = 0.08$ m. Numbers 1-6 indicate different flow passages, while letters A-F denote stall vortices near the impeller inlet and letters a-f represent stall vortices on pressure surfaces. For an outlet blade angle of 15° , stall vortices A-F are attached on suction

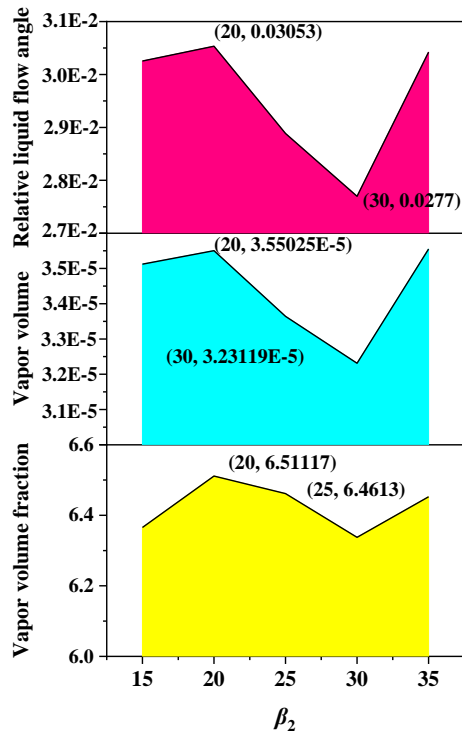


Fig. 10. Variations in the relative liquid flow angle, vapor volume, and vapor volume fraction.

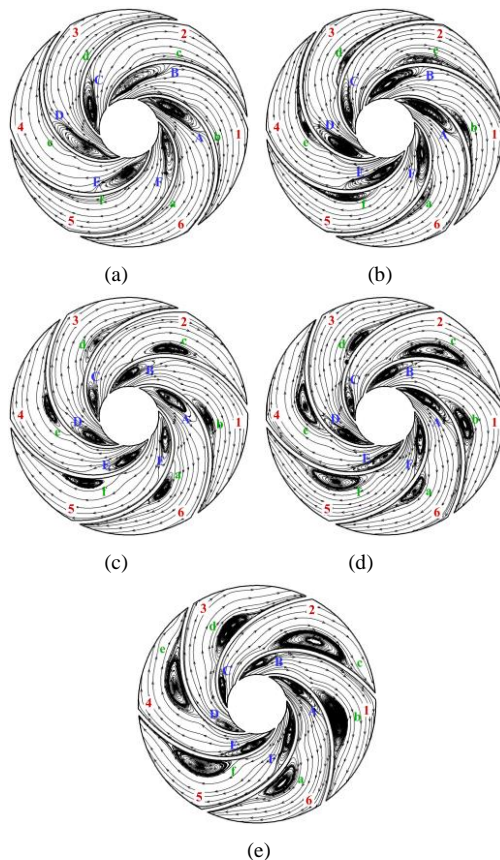


Fig. 11. Distributions of stall vortices in the impeller middle span ($NPSH_a = 0.08$ m) where β_2 is (a) 15°, (b) 20°, (c) 25°, (d) 30°, and (e) 35°.

surfaces. They are long and narrow along the flow direction of the passages. Stall vortices A and B are longer than one half of the blade length. Stall vortices at pressure surfaces begin to form and influence the flow fields; however, the distribution scope is small. For an angle of 20°, stall vortices A-F on the suction surfaces shrink along the flow direction, while the thickness increases. In contrast, stall vortices a-f on the pressure surfaces extend to the impeller outlet and are generally thin. When the angle is 25°, stall vortices A-F continue shrinking along the flow direction and decrease in thickness. The distribution scopes of stall vortices a-f become larger. With an angle of 30°, stall vortices A-F become slightly longer. The affected regions of stall vortices a-f continue to enlarge, especially in passage 2. At an angle of 35°, the distribution scopes of stall vortices C and D are smaller, whereas for the other vortices, variations are relatively slight. Meanwhile, the scopes of stall vortices a-f become the largest. Thus, comprehensive analyses reveal that stall vortices influence the smallest regions when the outlet blade angle is 25°.

5.3 Variations in Pressure Fluctuation

From section I to section VIII (Fig. 12), eight points are arranged and labeled as $P_1, P_2, P_3, P_4, P_5, P_6, P_7,$ and P_8 . Pressure fluctuations at these points are monitored to investigate the effects of different outlet blade angles.

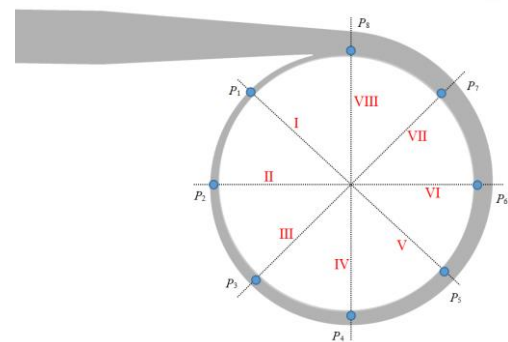


Fig. 12. Monitored pressure fluctuation points in different sections.

Figure 13 shows three-dimensional distributions of the pressure coefficient for all monitored points. Over time, the pressure coefficient at each monitored point shows periodicity with six maximal and minimal values, corresponding to the blade number. Fluctuations at P_1 are the strongest, and those at P_8 are the weakest. Pressure coefficient fluctuation decreases gradually from P_1 to P_8 . Owing to intense mutual interference between the rotating impeller and stationary volute, pressure fluctuations are mainly generated at the volute tongue; for P_1 and P_8 , they are closest to the volute tongue. Corresponding variations in the pressure coefficient are significant. However, the laws are different. The height of the volute channel at P_1 is only 7.1 mm, and therefore, when water is ejected from the impeller outlet to the volute (which is one

spiral structure), the kinetic energy of water instantly becomes potential pressure energy. Moreover, periodic collisions of water streams in the impeller channel cause intense fluctuations in the pressure in the volute. However, this pressure decreases as the volute channel area increases. Point P_8 is located at the volute channel outlet, and thus, the direction of high-energy water recovers by the volute does not change. As a result, pressure coefficient fluctuation is the weakest at this point.

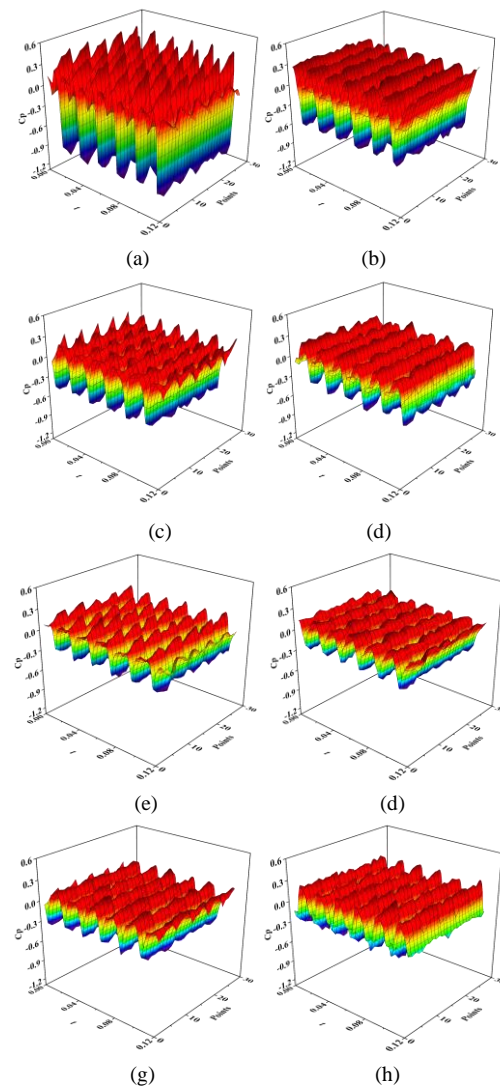


Fig. 13. Three-dimensional distributions of pressure coefficients at (a) P_1 , (b) P_2 , (c) P_3 , (d) P_4 , (e) P_5 , (f) P_6 , (g) P_7 , and (h) P_8 .

From the y-axis perspective, variations in pressure coefficient also show periodicity. The number of cycles corresponds to values of $NPSH_a$ (0.054, 0.080, 0.288, and 0.492 m). Under different $NPSH_a$ conditions, pressure coefficient fluctuations are consistent. As shown in Fig. 14, a few small cavitation bubbles form in the impeller channels. Therefore, they have negligible impacts on variations in the flow field, internal flow, or high-frequency energy. In contrast, these bubbles

increase the head, thereby further improving the hydraulic performance, as shown in Fig. 10. For P_1 , P_3 , P_5 , and P_7 , the pressure coefficient increases as the outlet blade angle increases. For P_2 , P_4 , P_6 , and P_8 , the corresponding variations are less significant.

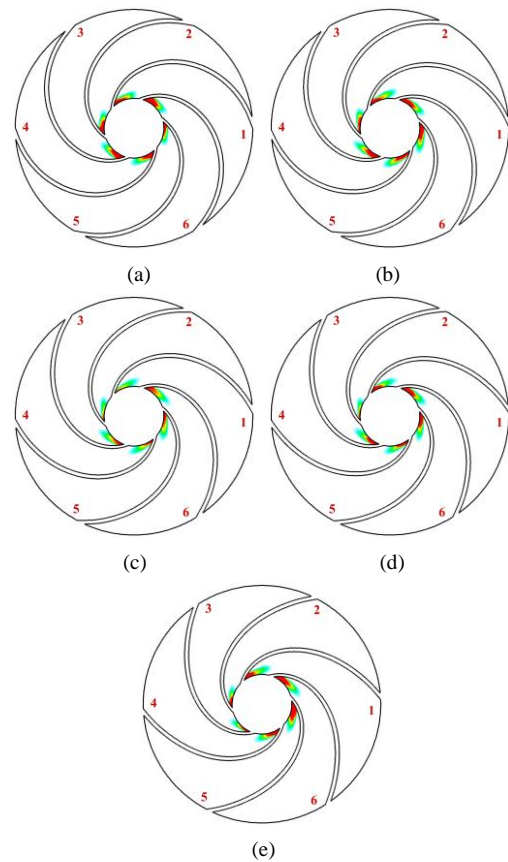


Fig. 14. Distributions of vapor volume fractions ($NPSH_a = 0.08$ m) where β_2 is (a) 15° , (b) 20° , (c) 25° , (d) 30° , and (e) 35° .

There are 30 points on the y-axis, and every five points comprise a group. Each point represents a different outlet blade angle (i.e., 15° , 20° , 25° , 30° , or 35°). There are also five groups that represent different cavitation development conditions (i.e., $NPSH_a = 0.054$, 0.080, 0.288, and 0.492 m or designed operating conditions).

The effects of cavitation on pressure fluctuations are reflected by the frequency. Therefore, variations in pressure at P_1 are analyzed via fast Fourier transform for $NPSH_a = 0.08$ m under designed operating conditions with different outlet blade angles. The results reveal the effects of cavitation on pressure pulsation energy. Spectra corresponding to P_1 under different outlet blade angles are shown in Fig. 15. There are clear differences in amplitude between 0-50 Hz under cavitation versus designed operating conditions (see points A, B, C, D, and E). Overall, the amplitude fluctuations under cavitation conditions are more significant. As the outlet blade angle increases, the amplitude also increases significantly because stall vortices attached to blade surfaces in the impeller channel distort the water trajectory. When high-

pressure water leaves the impeller outlet and enters the volute, it is impacted significantly. The water flow trajectory swing becomes more intense, which leads to irregular fluctuations of pressure. Meanwhile, the amplitude of the main frequency increases as the outlet blade angle increases. When the angle is 35°, it exceeds the amplitude of frequency doubling, which indicates that energy for frequency doubling is more stable. Although the energy for the main frequency is very unstable, it still occupies a dominant position. This is because the volute cross-domain is small, which induces a rapid change in energy when high-energy water enters the volute. As a result, amplitude distortion of the main frequency is observed.

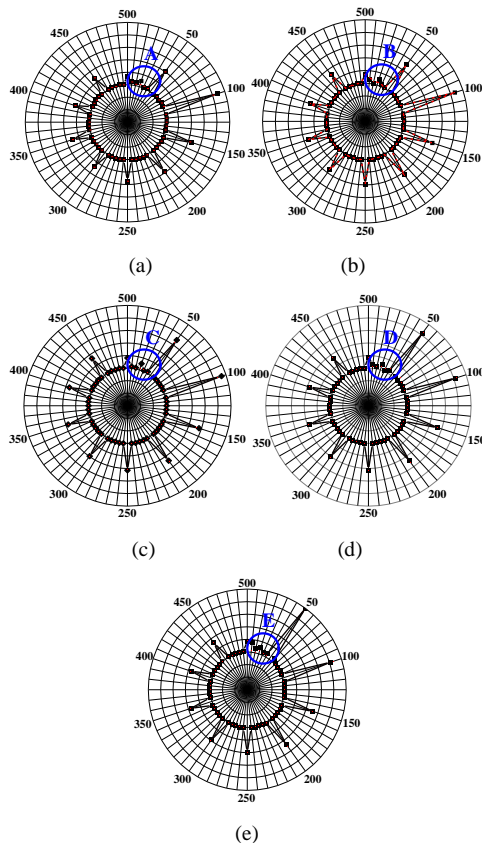


Fig. 15. Spectral diagrams of P_1 with outlet blade angles β_2 of (a) 15°, (b) 20°, (c) 25°, (d) 30°, and (e) 35°.

In Fig. 15, the radial direction represents amplitude (range = -0.15 to 0.25), and the circumferential direction corresponds to frequency (range = 0-500 Hz). Black lines indicate cavitation development conditions under $NPSH_a = 0.08$ m, and blue lines indicate designed operating condition.

5.4. Variations in Centrifugal Pump Stability

Cavitation compliance reveals the relationship between vapor volume and the absolute pressure of the monitored point, as defined in Eq. 8.

$$K = -\rho \frac{dV_c}{dp} \quad (8)$$

where K is cavitation compliance, V_c is vapor volume, p is the pressure of the monitored point (for our simulations, it is at the blade inlet).

This relationship is analyzed to evaluate the stability of the centrifugal pump under different cavitation development conditions. When $K \leq 0$, the pressure in the flow field decreases, causing bubbles to collapse. Then, the extra space is filled by water around the cavitation bubbles, thereby further reducing the pressure and causing the environment to deteriorate. Under these conditions, the centrifugal pump is unstable.

Figure 16 shows cavitation compliance variations in one cycle for different outlet blade angles. The compliance alternates, which indicates that cavitation bubbles induce unstable flow fields oscillations. When the outlet blade angle is 15° or 35°, K exhibits particularly significant variations. In one cycle, $K \leq 0$ at many instances, and thus, the centrifugal pump is especially unstable. At angles of 20° or 30°, the variations are relatively weaker and account for less time. When the angle is 25°, variations are the weakest and fewest, and the centrifugal pump is stable.

6. CONCLUSION

This study employs numerical simulations to investigate cavitation flow in centrifugal pumps with various outlet blade angles. Variations in hydraulic and cavitation performance of the centrifugal pump, stall vortices in the impeller middle span, pressure fluctuations in the volute, and cavitation compliance are discussed to evaluate the effects of the outlet blade angle on a centrifugal pump's internal flow field characteristics. The main conclusions from this work are as follows:

(1) Under both designed operating and cavitation conditions, head increases and efficiency decreases as the outlet blade angle increases. The relative liquid flow angle, vapor volume, and corresponding volume fraction first increases, then decreases, and finally increases again as the outlet blade angle increases.

(2) As the outlet blade angle increases, the distribution scopes of stall vortices on suction surfaces become smaller, then larger, and smaller again. Meanwhile, the scopes of vortices on pressure surfaces continuously increase.

(3) At the volute inlet, pressure fluctuations at all monitored points become weaker over time. Variations in pressure fluctuations alternate as the outlet blade angle increases.

(4) The amplitude of the main frequency increases and that of frequency doubling decreases as the outlet blade angle increases.

(5) As the outlet blade angle increases, the time during which cavitation compliance is less than 0 first decreases and then increases.

(6) When the outlet blade angle is 25°, centrifugal pump achieves its best performance: it

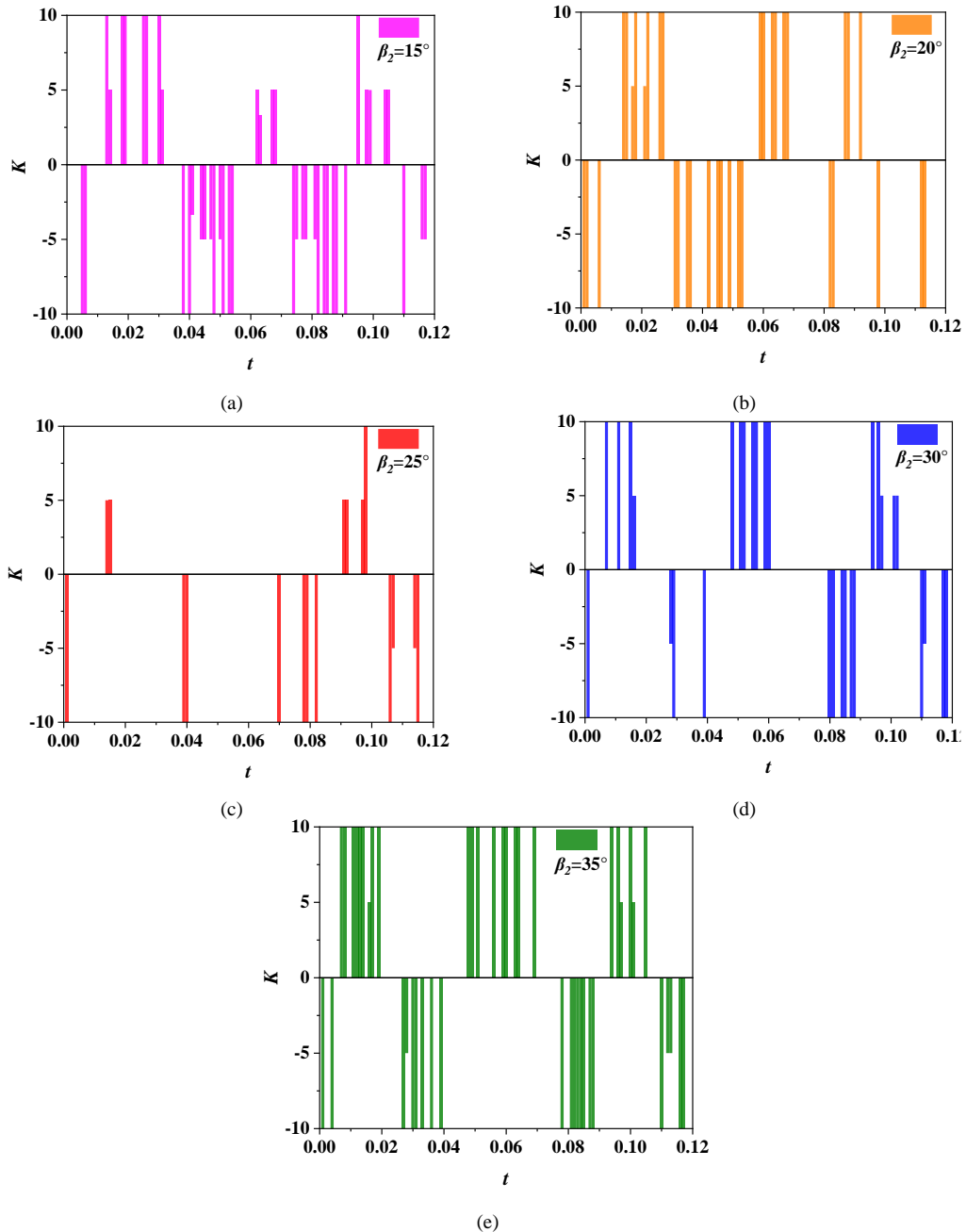


Fig. 16. Variations in cavitation compliance for outlet blade angles β_2 of (a) 15° , (b) 20° , (c) 25° , (d) 30° , and (e) 35° .

has the smallest distribution scopes of stall vortices and the fewest moments when cavitation compliance is less than 0.

ACKNOWLEDGEMENTS

The investigation was financially supported by National Natural Science Foundation of China (Grant No. 52169018).

REFERENCES

Bacharoudis, E. C., A. E. Filios, M. D. Mentzos and D. P. Margaris (2008). Parametric study of

a centrifugal pump impeller by varying the outlet blade angle. *The Open Mechanical Engineering Journal* 2(1), 75-83.

Biryukov, D., D. Gerasimov and E. Yurin (2022). *Cavitation and Associated Phenomena*. Boca Raton: CRC Press.

Bozorgasareh, H., J. Khalesi, M. Jafari and H. O. Gazori (2021). Performance improvement of mixed-flow centrifugal pumps with new impeller shrouds: Numerical and experimental investigations. *Renewable Energy* 163(Aug.), 635-648.

Chen, X. B., R. H. Zhang and W. F. Yang (2022).

- Inverse design and optimization of low specific speed centrifugal pump blade based on adaptive pod hybrid model. *Journal of Applied Fluid Mechanics* 15(2),453-464.
- Coutier-Delgosha, O., R. Fortes-Patella and J. L. Reboud (2003). Evaluation of the turbulence model influence on the numerical simulations of unsteady cavitation. *Journal of Fluids Engineering-Transactions of the ASME* 125(1), 38-45.
- Decaix, J. and E. Goncalves (2013). Compressible effects modeling in turbulent cavitating flows. *European Journal of Mechanics-B/Fluids* 39(39), 11-31.
- Donmez, A. H., Z. Yumurtaci and L. Kavurmacioglu (2019). The effect of inlet blade angle variation on cavitation performance of a centrifugal pump: A Parametric Study. *Journal of Fluids Engineering* 141(2), 021101.
- Dular, M., R. Bachert, C. Schaad and B. Stoffel (2007). Investigation of a re-entrant jet reflection at an inclined cavity closure line. *European Journal of Mechanics-B/Fluids* 26(5), 688-705.
- Elyamin, G. R. H. A., M. A. Bassily, K. Y. Khalil and M. S. Gomaa (2019). Effect of impeller blades number on the performance of a centrifugal pump. *Alexandria Engineering Journal* 58, 39-48.
- Ennouri, M., H. Kanfoudi, A. Bel Hadj Taher and R. Zgolli (2019). Numerical flow simulation and cavitation prediction in a centrifugal pump using an SST-SAS turbulence model. *Journal of Applied Fluid Mechanics* 12(1), 25-39.
- Ferziger, J. H., M. Peric and R. L. Street (2019). *Computational Methods for Fluid Dynamics*. Berlin: Springer.
- Grist, E (1998). *Cavitation and the Centrifugal Pump: A Guide for Pump Users*. Boca Raton: CRC Press.
- Matlakala, M. E., D. V. V. Kallon, K. E. Mogapi, I. M. Mabelane and D. M. Makgopa (2019). Influence of impeller diameter on the performance of centrifugal pumps. *IOP Conference Series: Materials Science and Engineering* 655(1), 012009.
- Mohammadi, N. and M. Fakhrazadeh (2017). Analysis of effect of impeller geometry including outlet blade angle on the performance of multi-pressure pumps: Simulation and Experiment. *Mechanika* 23(1), 107-119.
- Peng, G. J., Q. Chen, L. Zhou, B. Pen and Y. Zhu (2020). Effect of Blade Outlet Angle on the Flow Field and Preventing Overload in a Centrifugal Pump. *Micromachines* 11(9), 811-822.
- Shi, W. D., L. Zhou, W. G. Lu, B. Pei and T. Lang (2013). Numerical prediction and performance experiment in a deep-well centrifugal pump with different impeller outlet width. *Chinese Journal Of Mechanical Engineering* 26(1), 46-52.
- Shigemitsu, T., J. Fukutomi and K. Kaji (2011). Influence of outlet blade angle and blade thickness on performance and internal flow conditions of mini centrifugal pump. *International Journal of Fluid Machinery and Systems* 4(3), 317-323.
- Shojaeefard, M. H., M. Tahani, M. B. Ehghaghi, M. A. Fallahian and M. Beglari (2012). Numerical study of the effects of some geometric characteristics of a centrifugal pump impeller that pumps a viscous fluid. *Computers & Fluids* 60(Feb.), 61-70.
- Su, X., W. Jin, Z. Zu, Z. Li and H. Jia (2021). Performance characteristics and energy loss analyses of a high-speed centrifugal pump with straight blades. *Journal of Applied Fluid Mechanics* 14(5), 1377-1388.
- Tu, J. Y., G. H. Yeoh and C. Q. Liu (2007). *Computational Fluid Dynamics: A Practical Approach*. Netherlands: Elsevier.
- Wang, T., X. B. Liu, X. D. Lai and Q. Q. Gou (2016). Effects of blade inlet width on performance of centrifugal pump as turbine with special impeller using in turbine mode, *ASME 2016 Fluids Engineering Division Summer Meeting*.
- Wilcox, D. C. (1994). Simulation of transition with a two-equation turbulence model. *AIAA Journal* 32(2), 247-255.
- Wilcox, D. C. (2008). Formulation of the $k-\omega$ turbulence model revisited. *AIAA Journal* 46(11), 2823-2838.
- Zhang, H. L., F. Y. Kong, A. X. Zhu, F. Zhao and Z. F. Xu (2020). Effect of outlet blade angle on radial force of marine magnetic drive pump. *Shock and Vibration*, 2020(Sep.), 1-18.
- Zwart, P. J., A. Gerber and G. Belamri (2004). A Two-Phase Flow Model for Predicting Cavitation Dynamics, *Proceedings of the Fifth international conference on multiphase flow, Yokohama, Japan*, 152, 11.